npj | 2D materials and applications

Article

Published in partnership with FCT NOVA with the support of E-MRS

https://doi.org/10.1038/s41699-025-00602-z

Programmable phonon-assisted resonant energy transfer between moiré cells in charge-tunable $MoSe_2$-WS_2 heterobilayers

Philipp Parzefall[1], Nicolas Paulik[1], Caique Serati de Brito[2,8], Jonas Göser[3,4], Julian Trapp[3,4], Kenji Watanabe[5], Takashi Taniguchi[6], Daniel Erkensten[7], Giuseppe Meneghini[7], Yara Galvão Gobato[2], Ermin Malic[7], Alexander Högele[3,4] & Christian Schüller[1] ✉

Moiré superlattices in van-der-Waals heterostructures offer a versatile platform for exploring emergent quantum phenomena. In type-I $MoSe_2$-WS_2 moiré superlattices, the large lattice mismatch ensures robustness of the moiré period against twist-angle disorder. The excitonic ground state is formed by moiré-trapped $MoSe_2$ intralayer excitons. However, a key challenge is the controlled transfer of excitonic energy across moiré sites. This work investigates gate-controlled phonon-assisted resonant energy transfer (RET) as a means to transfer excitonic energy between moiré cells. By harnessing the interplay between resonantly excited moiré excitonic complexes and single or few phonons, energy transfer pathways can be modulated via the charging state of moiré cells. We discuss two potential RET mechanisms: phonon-assisted resonant tunneling and Förster-like dipole–dipole transfer. Our findings highlight the potential of this approach for excitonic circuits and nanoscale energy transport, paving the way for future applications in quantum technologies.

Van-der-Waals (vdW) materials offer exciting opportunities to engineer novel compounds with precisely controlled layer numbers, compositions, and vertical alignments. A key focus in current research is the impact of moiré superlattices, which emerge from stacking layers with different lattice constants and twist angles[1–3]. Moiré superlattices in transition-metal dichalcogenide (TMDC) heterobilayers provide a powerful platform for studying quantum phenomena, including correlated electronic states[4–14] and exciton physics[15–28]. Notably, selenide-sulfide heterobilayers – such as $MoSe_2$-WS_2 and WSe_2-WS_2 – are particularly valuable due to their significant lattice mismatch (approx. 3−4%), which enhances superlattice stability against local twist-angle variations[1,3].

Recent studies on $MoSe_2$-WS_2 and WSe_2-WS_2 heterobilayers have, e.g., revealed correlated insulating states at integer and fractional moiré lattice fillings via quantum capacitance[4,9] and reflectance contrast (RC) measurements[7]. In $MoSe_2$-WS_2 it was found that an electron-doped Mott state (filling factor $\nu = 1$) exhibits ferromagnetic correlations, consistent with the Nagaoka mechanism[14]. Charged intralayer moiré excitons were investigated in WSe_2-WS_2 heterobilayers[15]. Additionally, quantum-confined Stark effect tuning of layer-hybridized states was demonstrated in WSe_2-WS_2[23], and higher-energy moiré exciton states were observed in $MoSe_2$-WS_2 using photoluminescence (PL) and RC spectroscopy[26]. Furthermore, it was reported that strong out-of-plane electric fields can induce a transition from type-I to type-II band alignment in $MoSe_2$-WS_2[29]. Unlike most TMDC heterobilayers, $MoSe_2$-WS_2 naturally exhibits type-I band alignment, confining moiré-trapped excitons primarily to the $MoSe_2$ layer[23–26]. However, a fundamental challenge remains: how to efficiently control energy transfer between moiré-trapped excitons.

In this work, we show that phonon-assisted resonant energy transfer (RET) offers a compelling mechanism for mediating excitonic energy transfer between moiré cells through lattice vibrations. While RET is well-

[1]Institut für Experimentelle und Angewandte Physik, Universität Regensburg, Regensburg, Germany. [2]Physics Department, Federal University of São Carlos, São Carlos, SP, Brazil. [3]Fakultät für Physik, Munich Quantum Center, and Center for NanoScience (CeNS), Ludwig-Maximilians-Universität München, München, Germany. [4]Munich Center for Quantum Science and Technology (MCQST), München, Germany. [5]Research Center for Electronic and Optical Materials, National Institute for Materials Science, Tsukuba, Japan. [6]Research Center for Materials Nanoarchitectonics, National Institute for Materials Science, Tsukuba, Japan. [7]Department of Physics, Philipps-Universität Marburg, Marburg, Germany. [8]Present address: Center for Information Technology Renato Archer (CTI Renato Archer), Campinas, SP, Brazil. ✉e-mail: christian.schueller@ur.de

established in molecular and solid-state systems (see, e.g., refs. 30–33), its programmability and tunability in moiré heterostructures remain largely unexplored. We demonstrate that by leveraging the interplay between resonantly excited, moiré-trapped excitons and single or few phonons, energy transfer pathways can be engineered and externally controlled via applied gate voltage. This study aims to shed light on the mechanisms governing programmable phonon-assisted RET in $MoSe_2$-WS_2 moiré superlattices, emphasizing its potential for excitonic circuits and energy-efficient nanoscale information transfer.

Results

Device characteristics

We prepared a series of 0° (R-type) and 60° (H-type) twisted (cf. Fig. 1a) $MoSe_2$-WS_2 heterobilayer samples using a deterministic all-dry transfer process (see "Methods"). This study focuses on four R-type devices, a dual-gate device is schematically illustrated in Fig. 1b, with a microscope image of an actual sample (sample R8) shown in Fig. 1c. Additionally, two H-type samples (H3, H4) without graphite gates serve as a comparison. The main part of this work examines a prototypical dual-gated R-type device (R8, Fig. 2c), while results from other samples with one gate (R6, R9, R10) are presented in the supplementary information. An experimental verification of the stacking type of sample R8 is provided in Supplementary Note 1.

Due to the ~4% lattice mismatch between $MoSe_2$ and WS_2, a moiré superlattice with a period of ~7.5 nm forms at a 0° twist (schematic in Fig. 1d). The lowest-energy excitons are intralayer A excitons in $MoSe_2$ (Fig. 1e)[23–26]. The real-space moiré superlattice gives rise to a mini Brillouin zone in reciprocal space (Fig. 1f), leading to a miniband structure for the $MoSe_2$ A excitons at the K points of the monolayer Brillouin zone in a continuum model[18]. However, local strain in the vicinities of high symmetry stacking points (e.g., R_h^M, R_h^X, R_h^h, cf. Fig. 1g, applying the notation of ref. 34) leads to two different exciton-potential minima for localization of $MoSe_2$ A excitons[14,35], labeled M_1 and M_2 in Fig. 1g, within a moiré cell at positions R_h^h and R_h^X. The spatial distribution of their wavefunctions, as calculated in ref. 26, show that, while M_1 is tightly localized, M_2 has a non-negligible spatial extent.

Gate-dependent photoluminescence and white-light reflectance contrast

We begin by characterizing our sample, with all measurements conducted at $T \sim 5$ K, unless otherwise stated. Heatmaps of the PL and the negative first derivative of the RC spectra, -d/dE(RC), as functions of symmetrically applied gate voltages on the bottom and top gates, are shown in Fig. 2b, c, respectively. Figure 2a displays PL spectra for selected filling factors. The PL is excited using a 532-nm laser, while RC measurements employ a white-light source (see "Methods"). In the charge-neutral regime ($\nu \sim 0$), we identify moiré excitons (M_1, M_2, see also Supplementary Note 1), as well as attractive (M_1^*) and repulsive (M_2^*) moiré Fermi polarons near a filling factor of $\nu \sim 1$. Furthermore, additional, presumably double-charged moiré polarons (M_1^{**}, M_2^{**}) emerge around a filling factor of 2 (Fig. 2a, c, d).

For gated $MoSe_2$-WS_2 heterobilayers, the spectral characteristics and energy spacings of moiré excitons at filling factors $\nu = 0$ and $\nu = 1$ - corresponding to neutral moiré excitons (M_1, M_2) and moiré Fermi polarons (M_1^*, M_2^*), respectively - are well documented.

For example, ref. 26 (as well as refs. 35,36) reports the observation of up to three neutral moiré excitons (M_1, M_2, and M_3) at $\nu = 0$, with comparisons made between R-type and H-type stacking. The ~35 meV energy spacing between M_1 and M_2 observed in Fig. 2 closely matches the values reported in ref. 26 for R-type $MoSe_2$-WS_2 heterobilayers. Additionally, the large energy gap between M_2 and M_3 observed in our sample R8 (see Supplementary Note 1) further confirms its R-type stacking and pinpoints the charge-neutral region corresponding to $\nu = 0$.

The energetic positions and spacings of features identified as M_1^* and M_2^* in our RC spectra (Fig. 2c, e) show near-quantitative agreement with those reported by Ciorciaro et al.[14] at $\nu = 1$ in a comparable dual-gated R-type $MoSe_2$-WS_2 heterobilayer (see their Fig. 1b and Extended Data 2). This strong consistency between our RC and PL measurements and the literature data from refs. 14,26,35,36 validates our assignments of M_1, M_2, M_1^*, and M_2^*, and supports our identification of the corresponding gate voltages.

Notably, M_1^{**} is very faint in RC (Fig. 2c), and in PL it appears clearly for higher positive gate voltages, i.e., $\nu > 2$, only (Fig. 2a). In Supplementary Note 2, we show a more detailed gate-voltage dependence of M_1^{**}. For M_1^{**} and M_2^{**}, hybridization with the WS_2 conduction band may play a role: PL measurements over a broader energy range, including the WS_2 PL (supplementary Fig. S4), suggest that for $\nu > 1$, the WS_2 conduction band minima become significantly populated, potentially indicating conduction-band hybridization. In ref. 36 it was speculated that the second electron may be localized in the higher potential minimum in the moiré cell, at site R_h^X, due to Coulomb repulsion. Similar behavior was reported in ref. 28 for hole-doping in WSe_2-WS_2 moiré superlattices. Since hybridization with the WS_2

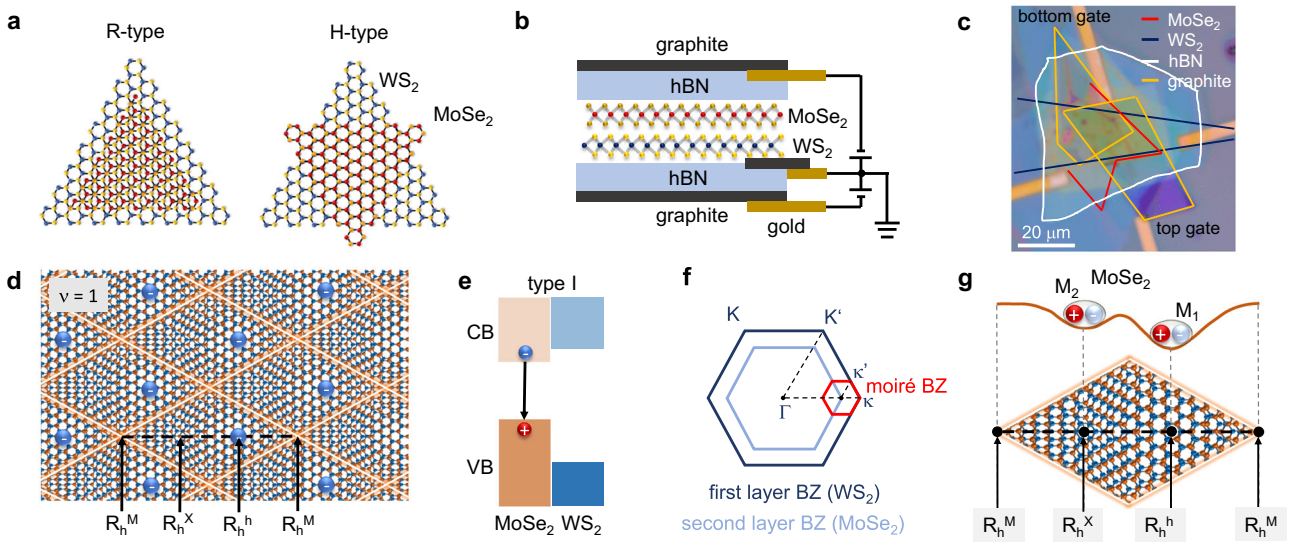

Fig. 1 | $MoSe_2$-WS_2 heterobilayer. a Lattice stackings for R-type and H-type TMDC heterobilayers. **b** Schematic of the investigated R-type $MoSe_2$-WS_2 device with two graphite gates. **c** Optical microscope image of our sample (R-type sample R8). **d** Moiré lattice with one electron per moiré cell (filling factor $\nu = 1$). High-symmetry stacking sites are indicated. **e** Schematic of the type-I band alignment of $MoSe_2$-WS_2 heterobilayers. **f** Brillouin zones of the two layers of an R-type structure, and the resulting mini Brillouin zone of the heterobilayer. **g** Schematic of the potential profile for *excitons* along the horizontal black dashed line. Two different moiré-trapped excitons are labeled M_1 and M_2.

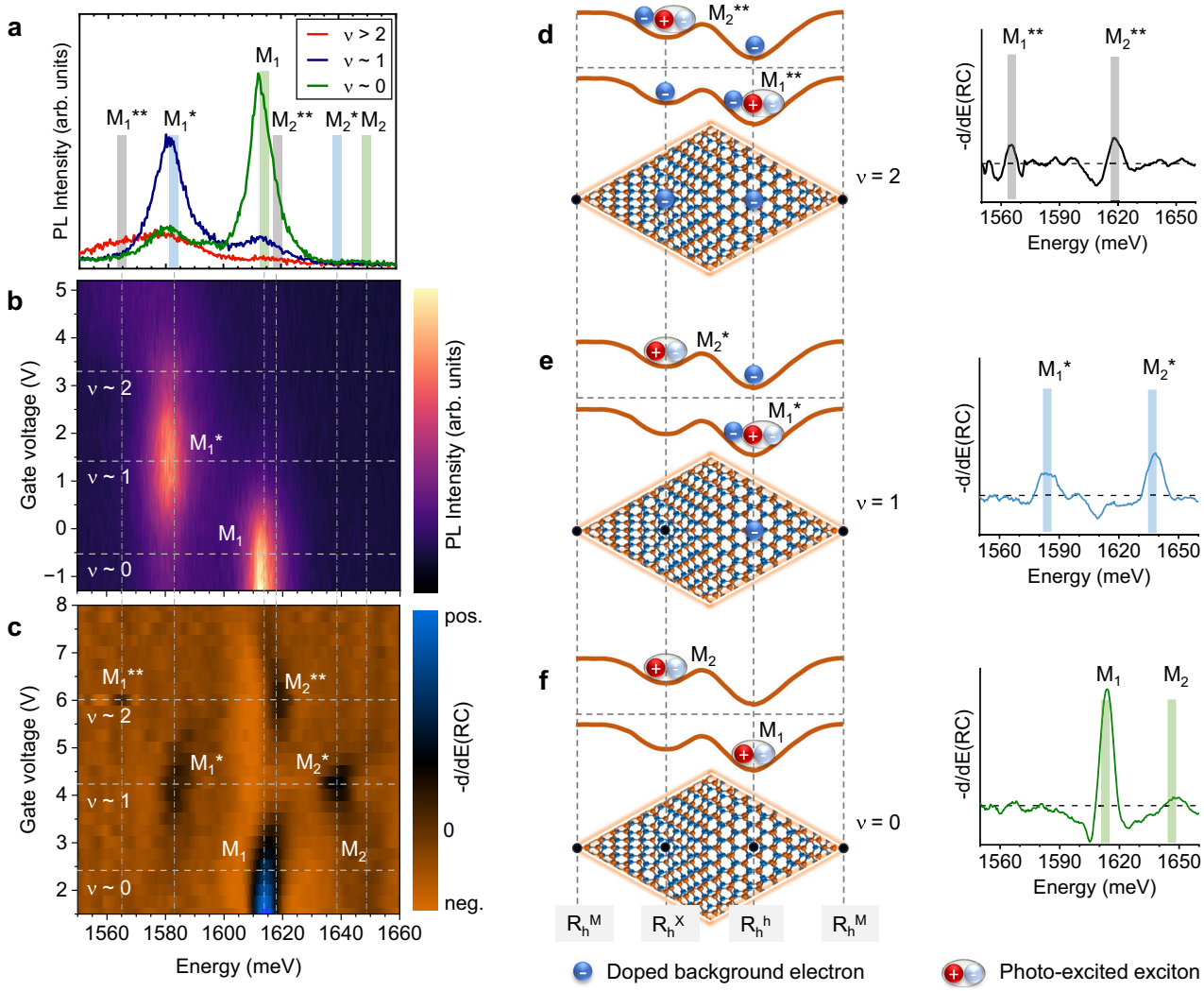

Fig. 2 | Moiré-trapped excitonic complexes in R-type heterobilayer. a Selected PL spectra from **b**. The vertical colored bars mark the positions of the moiré excitonic complexes, extracted from (**b**, **c**). **b** Heatmap of PL spectra versus gate voltage. **c** Heatmap of the negative derivative of RC spectra versus gate voltage. **d**–**f** Schematic of moiré-trapped excitonic complexes, together with the locations of doped charges at high symmetry sites in the moiré cell, and corresponding differential RC spectra, extracted from **c**: For **d** a double-charged exciton M_2^{**} at filling factor $\nu \sim 2$, **e** ground state (M_1^*) and excited-state (M_2^*) single-charged exciton at filling factor $\nu \sim 1$, and, **f** ground-state (M_1) and excited-state (M_2) neutral exciton at filling factor $\nu \sim 0$.

conduction band is more significant for the higher energy minimum[26,36], our assumption for the charge arrangement for M_1^{**} and M_2^{**} in the schematic in Fig. 2d is reasonable, keeping in mind possible complications due to hybridization with the WS_2 conduction band for filling factor $\nu > 1$. Overall, the assignment of M_1^{**} and M_2^{**} is speculative at the moment and requires further verification. However, this is not the focus of this work and does not influence our main conclusions.

The excitonic complexes are schematically illustrated in Fig. 2d–f using potential profiles for neutral excitons, as calculated in ref. 26 for similar R-type moiré lattices. The additional background electrons are just schematically superimposed in Fig. 2d, e, since they are localized at the corresponding high-symmetry stacking sites (cf. refs. 28,36). If the moiré-trapped excitonic complexes are sufficiently localized, it is appropriate to refer to them as moiré excitons and trions rather than repulsive and attractive polarons[14]. We will adopt this notation throughout. Alongside the schematics in Fig. 2d–f, selected -d/dE(RC) spectra from Fig. 2c are shown. In particular, Fig. 2f highlights the first excited moiré exciton (M_2), which appears faint in Fig. 2c but is more discernible here. A more detailed investigation is provided in Supplementary Note 1.

Notably, for all R-type samples, we consistently observe a rigid gate-voltage difference of ~3 V between nonresonant PL and RC measurements for similar filling factors, across different measurement runs (cf. Fig. 2b, c). This effect is highly reproducible, though its origin remains unclear. It also persists when a long-pass optical filter is applied to the white-light continuum in RC measurements. Furthermore, we can only tune to the electron-doped regime at positive gate voltages for most situations at low temperatures. For negative voltages, the structures mostly remain charge neutral over a large voltage range of at least 0 to −8 V. A detailed analysis of the homogeneity of the investigated sample, as well as the procedure of determining the filling factors for the different experiments, are provided in the supplementary information (Supplementary Notes 3 and 4).

The PL spectra in Fig. 2a indicate some degree of inhomogeneity in our sample, as approximately 16% of the PL signal at optimal gate voltages for filling factors of 0 or 1 originates from the opposite filling factor. For instance, at $\nu \sim 1$, about 84% of moiré cells are correctly charged with one electron, producing the blue M_1^* PL line in Fig. 2a, while 16% remain unoccupied, contributing to the blue M_1 PL line. The reverse holds for $\nu \sim 0$ (green PL lines in Fig. 2a).

Phonon-assisted resonant energy transfer

Next, we focus on the core of our investigation: phonon-assisted RET between moiré cells. To explore this, we perform near-resonant PL experiments using a tunable continuous-wave Ti:Sapphire laser to excite excitonic complexes resonantly ("Methods"). Figure 3a presents a heatmap of near-resonantly excited PL spectra for $\nu \sim 0$. The y-axis represents the excitation laser energy, while the x-axis shows the energy redshift relative to the laser, a convention typical for Stokes Raman plots. Faint vertical lines (marked by small white arrows) correspond to Stokes phonon Raman scattering of the out-of-plane A_{1g} (~30 meV) and in-plane E^1_{2g} (~36 meV) $MoSe_2$ phonons, characterized by a constant energy shift. In contrast, PL lines shift in these plots, as indicated by dashed lines with finite slopes for M_1 (~1612 meV) and M_1^* (~1574 meV). At $\nu \sim 0$, the charge-neutral moiré exciton M_1 exhibits strong resonance fluorescence at ~1612 meV. Due to sample inhomogeneity, some moiré sites remain singly charged, leading to the excitation of M_1^* when M_1 is resonantly excited, marked by a purple bullet in Fig. 3a. On the other hand, when resonantly exciting M_2^* and M_2, maxima occur (marked by orange and gray bullets, respectively), which require integer filling factors.

The energy separations between M_1 and M_1^*, and between M_2 and M_1, approximately match phonon energies of $MoSe_2$ (see supplementary Fig. S9 for nonresonant Raman spectra of monolayers and the heterobilayer). The separation between M_2^* and M_1^* corresponds to roughly twice the A_{1g} phonon energy, suggesting highly efficient down-conversion processes for $M_1 \rightarrow M_1^*$, $M_2^* \rightarrow M_1^*$, and $M_2 \rightarrow M_1$. Phonon-assisted up-conversion, so called excitonic Antistokes PL, was reported for TMDC monolayers[37–39], and, recently, for twisted bilayer WSe_2[40]. In ref. 41, the transfer rates for phonon-assisted up- and down-conversion processes in TMDC monolayers were calculated, in dependence on parameters like temperature and doping density. In this work, we investigate down-conversion of excitonic complexes both within and between moiré cells. Unlike up- or down-conversion processes in monolayers, where the spatial separation between initial and final exciton states is not fixed[37–39], the moiré cells in our system impose well-defined spatial separations.

While $M_2 \rightarrow M_1$ and $M_2^* \rightarrow M_1^*$ occur primarily within or between moiré cells of the same charging state (Fig. 3c, d for $\nu \sim 0$ and $\nu \sim 1$, respectively), the $M_1 \rightarrow M_1^*$ transition requires exciton transfer between moiré cells of different charging state. This inter-cell transfer process is schematically illustrated in Fig. 3e: a neutral exciton M_1 is created in an uncharged cell, and scatters resonantly, by the emission of one phonon, to a neighboring cell, which is charged by one electron. In Fig. 3e, three of the possibilities with shortest distance are depicted. For this process, the spatial distance and potential height, which have to be overcome, are larger than for the inner/inter-cell processes in Fig. 3c, d. Complementary heatmaps for the other three investigated R-type samples (R6, R9, R10) are provided in supplementary Fig. S9. We note that one could in principle also think of the reversed processes in Fig. 3e, i.e., an electron from the neighboring cell tunneling into the cell, which is occupied by M_1. However, we believe that tunneling of the neutral exciton M_1 is more likely, since the doped electrons are more strongly locked in their positions, due to Coulomb repulsion with the other electrons[4].

Next, we compare measurements at a gate voltage near $\nu \sim 1$ (Fig. 3b). The resonance fluorescence of M_1 is significantly weaker than at $\nu \sim 0$. Consistently, the process $M_2 \rightarrow M_1$ (marked by a gray bullet in Fig. 3b) is no longer distinguishable from the diffuse background, in contrast to $\nu \sim 0$ (Fig. 3a). However, the process $M_2^* \rightarrow M_1^*$ becomes more pronounced at $\nu \sim 1$ (note the log. scale of the intensities in Fig. 3a, b, both plots have the same scale).

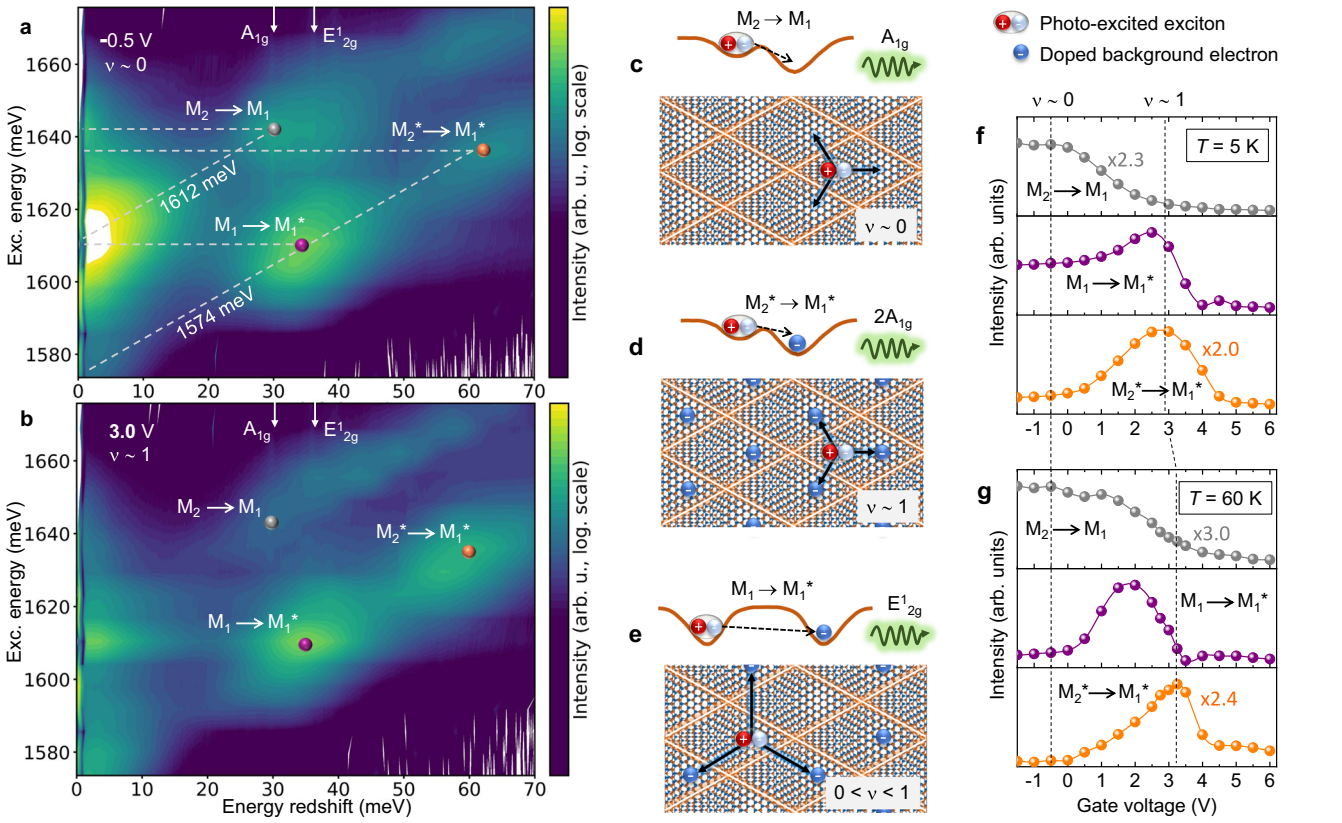

Fig. 3 | Resonantly-excited PL measurements of R-type heterobilayer. a Heatmap (log. scale) of resonantly-excited PL spectra versus energy shift with respect to the exciting laser, at -0.5 V gate voltage, applied symmetrically to both gates. Positions of specific energy transfer processes are labeled and marked by colored bullets. The small vertical arrows mark positions of $MoSe_2$ phonons. **b** Same as **a** but for 3.0 V gate voltage. **c–e** Schematic of phonon-assisted resonant energy transfer within a moiré cell and between neighboring moiré cells. **f** PL intensities at positions, indicated by bullets of the same color in (**a**, **b**) versus gate voltage at $T = 5$ K. **g** Same as (**f**) but for $T = 60$ K.

In the following, we analyze the gate-voltage dependence of the RET processes in greater detail. Figure 3f, g show the intensity variations of these processes as a function of gate voltage, extracted from a series of measurements at $T = 5$ K and $T = 60$ K, including the examples in Fig. 3a, b.

The observed trends further support our interpretation. We begin with the data for $T = 5$ K (Fig. 3f): the process $M_2 \rightarrow M_1$ is maximal at $\nu \sim 0$, persists at negative gate voltages, and decreases towards $\nu \sim 1$. As noted earlier, at negative gate voltages, the heterobilayer remains in a charge-neutral state, though some of the cells remain charged due to inhomogeneity. Therefore, the inter-cell process $M_1 \rightarrow M_1^*$ has some finite strength at $\nu \sim 0$ before becoming maximal towards $\nu \sim 1$. This is somehow surprising, since we would expect the maximum for this process for a filling factor $\nu \sim 1/2$, when a maximum of charged and uncharged moiré cells are next to each other (Fig. 3e). The process $M_2^* \rightarrow M_1^*$ shows a clear maximum at $\nu \sim 1$.

It appears that the charging of the moiré cells is more homogeneous, when the sample temperature is raised to some extent. To show this, Fig. 3g displays the intensities for a temperature of $T = 60$ K. Now, the inter-cell process $M_1 \rightarrow M_1^*$ shows a clear maximum between filling factors $\nu \sim 0$ and $\nu \sim 1$ and is small at integer fillings. Similarly, the maximum of $M_2^* \rightarrow M_1^*$ at $\nu \sim 1$ is better pronounced. The gate-voltage positions of the filling factors $\nu \sim 0$ and $\nu \sim 1$ in Fig. 3f, g are determined by the positions of the maxima of the resonance fluorescence of M_2 and M_2^*, respectively (see Supplementary Note 4).

For direct comparison of transition probabilities, we normalize the raw spectra intensities to the corresponding intensities of the resonance fluorescence tails at a small energy shift of 3.5 meV. For this, we assume that the probability for direct recombination - as a first-order process - is much higher than that for a phonon-assisted energy transfer, which is at least of second order. This gives us a rough estimate for the relative probabilities of the RET processes, since their number depends on the number of excited initial states. We do this for a gate voltage of 1.0 V, i.e., for $0 < \nu < 1$, where all discussed transitions are present. The resulting heatmap, shown in Fig. 4a, reveals that the processes $M_2 \rightarrow M_1$ and $M_2^* \rightarrow M_1^*$, which both can take place within a moiré cell, are significantly more efficient than the inter-cell process $M_1 \rightarrow M_1^*$, which is hardly discernable from the background. This supports our interpretation of the RET processes, since for the inter-cell process, the transfer has to bridge a larger spatial distance (cf. Fig. 3c–e).

Discussion

Finally, we discuss two likely mechanisms for RET: (i) phonon-assisted resonant tunneling and (ii) phonon-assisted Förster resonance energy transfer. For all three processes - $M_2 \rightarrow M_1$, $M_2^* \rightarrow M_1^*$ and $M_1 \rightarrow M_1^*$ - the energy differences between the initial and final states correspond to one or two phonon energies of the $MoSe_2$ lattice. Thus, with the simultaneous emission of one or two phonons, these processes become energetically resonant. The electron-phonon interaction matrix element, which is essential for phonon-assisted RET, was theoretically predicted in ref. 41 to decrease with increasing temperature for TMDC monolayers with background doping. However, this decrease primarily results from the Fermi energy smearing of free electrons at higher temperatures[41]. Since this effect may not be relevant for moiré-trapped electrons and M_1 excitons in our case, its impact remains uncertain.

The dependence of RET on spatial distance d differs for the two mechanisms: Tunneling follows a negative exponential dependence, while dipole–dipole coupling is proportional to $1/d^4$. This distinction could enable discrimination between the two mechanisms. However, achieving this would require a series of samples with varying twist angles, and consequently different moiré periods d – a task beyond the scope of this work.

To identify the relevant mechanism tentatively, we examine the temperature dependence of the $M_1 \rightarrow M_1^*$ process, which requires down-conversion between the most spatially separated excitonic complexes. Figure 4b shows the measured M_1^* intensities for this process as a function of gate voltage at four different temperatures. To minimize statistical

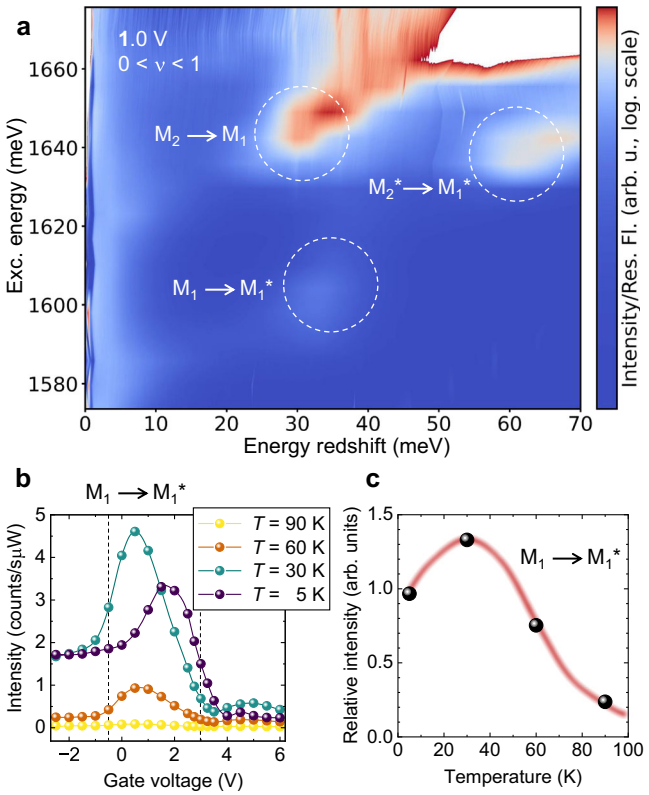

Fig. 4 | Relative intensities of resonantly-excited PL. a Heatmap (log. scale) of resonantly-excited PL for a gate voltage of 1.0 V, normalized to the intensities at an energy shift of 3.5 meV (Res. Fl.). **b** Intensitiy of the process $M_1 \rightarrow M_1^*$ versus gate voltage for four different temperatures. All data are averaged over measurements from five different spots on the sample. **c** Intensities of $M_1 \rightarrow M_1^*$, normalized to the intensities at an energy shift of 4 meV. The red line is a guide to the eye.

uncertainties, all measurements are repeated at five different sample locations, with the displayed data representing the averages for each gate voltage. The $M_1 \rightarrow M_1^*$ intensity reaches its maximum at $T \sim 30$ K, supporting our argument that increased temperature leads to a more homogeneous distribution of doped charges. We anticipate that for $T > 30$ K, within $0 < \nu < 1$, thermal energy in combination with Coulomb repulsion lead to a more homogeneous charging, resulting in a maximum number of unoccupied moiré minima adjacent to occupied ones. This enhances the $M_1 \rightarrow M_1^*$ signal. Furthermore, the finite thermal energy at elevated temperatures equilibrates energy inhomogeneities between moiré cells, which may also result in an increase in tunneling probabilities. Notably, the energies of TA and LA moiré phonons of $MoSe_2$ are for a superlattice period of ~7.5 nm about 2 meV and 3 meV[42], respectively, i.e., they are thermally-activated for $T \gtrsim 30$ K. In a higher-order process, this may also support the energy transfer between moiré cells.

Since the absolute number of transfer processes depends on the number of initially excited excitons, we normalize M_1^* intensities by those at an energy shift of 4 meV (i.e., the tail of M_1 resonance fluorescence), similar to Fig. 4a. The resulting relative-intensity maxima, which reflect process probabilities, are plotted against temperature in Fig. 4c. The data indicate that RET probability decreases with increasing temperature. As discussed above, we attribute the initial increase from 5 to 30 K to a more homogeneous charge distribution in the moiré lattice.

We assume that the moiré-trapped M_1 excitons are strongly localized. Recent theoretical predictions[43] suggest that the dipole–dipole coupling of excitons localized in a moiré lattice follows a power-law increase with temperature. This effect may contribute to the observed probability increase at low temperatures. However, an experimental study of the Förster transfer rate for interlayer exciton transfer between WS_2 and $MoSe_2$ found no

significant temperature dependence up to 200 K[30], indicating that Förster transfer cannot explain the overall temperature dependence observed in Fig. 4c.

At higher temperatures, exciton-phonon scattering becomes significant[43,44], and the reduced transfer efficiency may be understood within the polaron picture. Here, exciton-acoustic-phonon interactions renormalize exciton energies, leading to a temperature-dependent tunneling rate, which decreases with temperature[45].

Notably, the theoretical studies in refs. 43–45 focus on neutral excitons. Currently, we cannot conclusively determine the impact of the additional charges present in our moiré structures on the transfer processes. Thus, we only tentatively propose phonon-assisted tunneling as the primary mechanism for RET.

In conclusion, we present evidence of a phonon-assisted RET process between excitonic complexes in charge-tunable $MoSe_2$-WS_2 moiré superlattices. This process occurs within or between moiré cells of the same charging state, as well as between cells of different chargings. We demonstrate that the RET can be deterministically switched on or off via the applied gate voltage. Based on temperature-dependent experiments, we tentatively identify phonon-assisted resonant tunneling between moiré cells as the primary mechanism.

Methods

Device fabrication

Few-layer graphene and hBN flakes (NIMS) are exfoliated from bulk crystals under ambient conditions onto Si/SiO_2. All TMDC monolayers are grown by chemical-vapor deposition (at MCQST), except for WS_2 in samples R8 and R9, which are exfoliated. A poly-dimethyl-siloxane/polycarbonate stamp is used to stack the individual layers employing the hot pick-up technique[46] at a temperature of 125 °C. The resulting field-effect device is placed on a Si/SiO_2 target substrate with gold contact pads. The stack is released by melting the PC film at 175 °C, followed by chloroform soaking to remove the PC residue. Finally, the gold pads are bonded to alloy stripes, enabling electrostatic doping with DC-voltage sources (Keithley 2400). For this work, a total of 10 R-type samples are fabricated, where samples R6, R9, and R10 are working single-gate devices and R8 is a working dual-gate device. The ground of samples R8 and R9 is in contact with the WS_2 monolayer and the ground of samples R6 and R10 with both TMDC monolayers. Four additional H-type samples are fabricated without gates. All measurements are performed on samples R6, R8-R10 and H3-H4.

Optical spectroscopy

All optical experiment are conducted in a back-scattering geometry. The samples are mounted onto the cold finger of a continuous-flow cryostat, except for the nonresonant Raman measurements in ambient conditions. Unless stated otherwise, all experiments are conducted at a temperature of 5 K.

For nonresonant PL and Raman experiments, a 532-nm laser beam is focused onto a spot of ~1 µm diameter using a 100x microscope objective with NA = 0.7. The spectra of the nonresonant PL measurements are recorded by a grating spectrometer with Peltier-cooled CCD camera. They are integrated for 3 s−5 s with an excitation power of 25 µW. For the nonresonant Raman experiments, three Bragg-filters are used to reduce the Rayleigh-scattered light. The integration time is 30–180 s with an excitation power of 2.5 mW. For the RC measurements, a broad-band whitelight source is used, resulting in a spot diameter ~5 µm. For the RC measurements, an integration time of 10–20 s is used. The excitation power is about 1 µW for the full spectral range.

For the resonant PL experiments, a tunable cw Ti:Sapphire laser is used in combination with a tunable laser line filter. The laser beam is focused with a 100x microscope objective with NA 0.7 to a spot with a diameter of ~2 µm. Measurements are conducted at a laser power of 800 µW and the spectra are collected using a triple Raman spectrometer in substractive mode and a liquid-nitrogen-cooled CCD camera.

Data availability

Data sets generated during the current study are available from the corresponding author on reasonable request.

Received: 9 April 2025; Accepted: 18 August 2025;
Published online: 30 September 2025

References

1. Wilson, N. P., Yao, W., Shan, J. & Xu, X. Excitons and emergent quantum phenomena in stacked 2D semiconductors. *Nature* **599**, 383–388 (2021).
2. He, F. et al. Moiré patterns in 2D materials: a review. *Nano Lett.* **15**, 5944–5951 (2021).
3. Mak, K. F. & Shan, J. Semiconductor moiré materials. *Nat. Nanotechnol.* **17**, 686–693 (2022).
4. Regan, E. C. et al. Mott and generalized Wigner crystal states in WSe_2/WS_2 moiré superlattices. *Nature* **579**, 359–363 (2020).
5. Huang, X. et al. Correlated insulating states at fractional fillings of the WS_2/WSe_2 moiré lattice. *Nat. Phys.* **17**, 715–721 (2021).
6. Ghiotto, A. et al. Quantum criticality in twisted transition metal dichalcogenides. *Nature* **597**, 345–350 (2021).
7. Xu, Y. et al. Correlated insulating states at fractional fillings of moiré superlattices. *Nature* **587**, 214–219 (2020).
8. Li, T. et al. Continuous Mott transition in semiconductor moiré superlattices. *Nature* **597**, 350–355 (2021).
9. Li, T. et al. Charge-order-enhanced capacitance in semiconductor moiré superlattices. *Nat. Nanotechnol.* **16**, 1068–1074 (2021).
10. Pan, H. & Das Sarma, S. Interaction-driven filling-induced metal-insulator transitions in 2D moiré lattices. *Phys. Rev. Lett.* **127**, 096802 (2021).
11. Zhou, Y. et al. Bilayer Wigner crystals in a transition metal dichalcogenide heterostructure. *Nature* **595**, 48–53 (2021).
12. Padhi, B., Chitra, R. & Phillips, P. W. Generalized Wigner crystallization in moiré materials. *Phys. Rev. B* **103**, 125146 (2021).
13. Li, H. et al. Imaging two-dimensional generalized Wigner crystals. *Nature* **597**, 650–654 (2021).
14. Ciorciaro, L. et al. Kinetic magnetism in triangular moiré materials. *Nature* **623**, 509–514 (2023).
15. Naik, M. H. et al. Intralayer charge-transfer moiré excitons in van der Waals superlattices. *Nature* **609**, 52–58 (2022).
16. Zhang, C. et al. Moiré patterns, and 2D electronic superlattices in MoS_2/WSe_2 hetero-bilayers. *Sci. Adv.* **3**, e1601459 (2017).
17. van der Zande, A. M. et al. Tailoring the electronic structure in bilayer molybdenum disulfide via interlayer twist. *Nano Lett.* **14**, 3869–3875 (2014).
18. Alexeev, E. M. et al. Resonantly hybridized excitons in moiré superlattices in van der Waals heterostructures. *Nature* **567**, 81–86 (2019).
19. Jin, C. et al. Observation of moiré excitons in WSe_2/WS_2 heterostructure superlattices. *Nature* **567**, 76–80 (2019).
20. Seyler, K. L. et al. Signatures of moiré-trapped valley excitons in $MoSe_2$/WSe_2 heterobilayers. *Nature* **567**, 66–70 (2019).
21. Tran, K. et al. Evidence for moiré excitons in van der Waals heterostructures. *Nature* **567**, 71–75 (2019).
22. Brotons-Gisbert, M. et al. Spin-layer locking of interlayer excitons trapped in moiré potentials. *Nat. Mater.* **19**, 630–636 (2020).
23. Tang, Y. et al. Tuning layer hybridized moiré excitons by the quantum-confined Stark effect. *Nat. Nanotechnol.* **16**, 52–57 (2021).
24. Tang, Y. et al. Dielectric catastrophe at the Wigner-Mott transition in a moiré superlattice. *Nat. Commun.* **13**, 4271 (2022).
25. Galvão Gobato, Y. et al. Distinctive g-Factor of Moiré-Confined Excitons in van der Waals Heterostructures. *Nano Lett.* **22**, 8641–8647 (2022).
26. Polovnikov, B. et al. Field-induced hybridization of Moiré Excitons in $MoSe_2$/WS_2 heterobilayers. *Phys. Rev. Lett.* **132**, 076902 (2024).

27. Wang, X. et al. Intercell moiré exciton complexes in electron lattices. *Nat. Mater.* **22**, 599–606 (2023).
28. Park, H. et al. Dipole ladders with large Hubbard interaction in a moiré exciton lattice. *Nat. Phys.* **19**, 1286–1292 (2023).
29. Kistner-Morris, J. et al. Electric-field tunable Type-I to Type-II band alignment transition in $MoSe_2/WS_2$ heterobilayers. *Nat. Commun.* **15**, 4075 (2024).
30. Kozawa, D. et al. Evidence for fast interlayer energy transfer in $MoSe_2/WS_2$ heterostructures. *Nano Lett.* **16**, 4087–4093 (2016).
31. Hu, Z. et al. Trion-mediated förster resonance energy transfer and optical gating effect in WS_2/hBN/$MoSe_2$ heterojunction. *ACS Nano* **14**, 13470–13477 (2020).
32. Thompson, J. J. P., Gerhard, M., Witte, G. & Malic, E. Optical signatures of Förster-induced energy transfer in organic/TMD heterostructures. *npj 2D Mater. Appl.* **7**, 69 (2023).
33. Selig, M., Malic, E., Ahn, K. J., Koch, N. & Knorr, A. Theory of optically induced Förster coupling in van der Waals coupled heterostructures. *Phys. Rev. B* **99**, 035420 (2019).
34. Yu, H., Liu, G. B., Tang, J., Xu, X. & Yao, W. Moiré excitons: from programmable quantum emitter arrays to spin-orbit-coupled artificial lattices. *Sci. Adv.* **3**, e1701696 (2017).
35. Polovnikov, B. et al. Implementation of the bilayer Hubbard model in a moiré heterostructure. Preprint at https://doi.org/10.48550/arXiv.2404.05494 (2024).
36. Polovnikov, B. et al. Coulomb-correlated states of moiré excitons and charges in a semiconductor moiré lattice. Preprint at https://doi.org/10.48550/arXiv.2208.04056 (2022).
37. Jones, A. M. et al. Excitonic luminescence upconversion in a two-dimensional semiconductor. *Nat. Phys.* **12**, 323–327 (2016).
38. Wang, G. et al. Double resonant Raman scattering and valley coherence generation in monolayer WSe_2. *Phys. Rev. Lett.* **115**, 117401 (2015).
39. Hao, K. et al. Coherent and incoherent coupling dynamics between neutral and charged excitons in monolayer $MoSe_2$. *Nano Lett.* **16**, 5109–5115 (2016).
40. Dai, Y. et al. Phonon-assisted upconversion in twisted two-dimensional semiconductors. *Light Sci. Appl.* **12**, 6 (2023).
41. Ayari, S., Jaziri, S., Ferreira, R. & Bastard, G. Phonon-assisted exciton/trion conversion efficiency in transition metal dichalcogenides. *Phys. Rev. B* **102**, 125410 (2020).
42. Parzefall, P. et al. Moiré phonons in twisted $MoSe_2$-WSe_2 heterobilayers and their correlation with interlayer excitons. *2D Mater.* **8**, 035030 (2021).
43. Shentsev, A. M. & Glazov, M. M. Electromagnetic field assisted exciton diffusion in moiré superlattices. *Phys. Rev. B* **111**, 045301 (2025).
44. Meneghini, G., Brem, S. & Malic, E. Excitonic thermalization Bottleneck in Twisted TMD heterostructures. *Nano Lett.* **24**, 4505–4511 (2024).
45. Knorr, W., Brem, S., Meneghini, G. & Malic, E. Polaron-induced changes in moiré exciton propagation in twisted van der Waals heterostructures. *Nanoscale* **16**, 8996–9003 (2024).
46. Pizzocchero, F. et al. The hot pick-up technique for batch assembly of van der Waals heterostructures. *Nat. Commun.* **7**, 11894 (2016).

Acknowledgements

P.P. and C.S. acknowledge the financial support of the Deutsche Forschungsgemeinschaft (DFG, German Research Foundation) SFB 1277 (Project-ID 314695032, project B05). J.G., J.T. and A.H. acknowledge funding by the Deutsche Forschungsgemeinschaft (DFG, German Research Foundation) within the Priority Programme SPP 2244 2DMP and the Germany's Excellence Strategy EXC-2111-390814868 (MCQST). K.W. and T.T. acknowledge support from the JSPS KAKENHI (Grant Numbers 21H05233and 23H02052), the CREST (JPMJCR24A5), JST and World Premier International Research Center Initiative (WPI), MEXT, Japan. Y.G.G. acknowledges Fundação de Amparo a Pesquisa do Estado de São Paulo (FAPESP Grant 22/08329-0) and "Coordenação deAperfeiçoamento de Pessoal de Nível Superior" (CAPES)-Probral-DAAD program (Grant 88881.895140/2023-01).

Author contributions

C.S. and Y.G.G. conceived the study. N.P., P.P., C.S., A.H., J.G., and J.T. designed and fabricated the samples. P.P. and N.P. conducted the optical experiments. T.T. and K.W. provided the bulk hBN crystals. P.P., N.P., and C.S. processed and analyzed the data. P.P., N.P., A.H., E.M., D.E., G.M., C.S.B., Y.G.G., and C.S. discussed the data. C.S. and P.P. wrote the manuscript with input from all coauthors.

Funding

Open Access funding enabled and organized by Projekt DEAL.

Competing interests

P.P., N.P., C.S.B., J.G., J.T., K.W., T.T., D.E., G.M., E.M., A.H., and C.S. declare no financial or non-financial competing interests. Y.G.G. serves as Guest Editor of npj QuantumMaterials and had no role in the peer-review or decision to publish this manuscript. Y.G.G. declares no financial competing interests.

Additional information

Supplementary information The online version contains supplementary material available at https://doi.org/10.1038/s41699-025-00602-z.

Correspondence and requests for materials should be addressed to Christian Schüller.